THE JOURNAL OF PHYSICAL CHEMISTRY LETTERS
A JOURNAL OF THE AMERICAN CHEMICAL SOCIETY

pubs.acs.org/JPCL

Letter

Ultrafast Electron–Dipole Interactions in TeO^- Photodetachment

Fan Yang, Haomai Hou, Jian Zhang, Xueying Li, Peng Tang, Ye Mei, Junyang Ma, Zhubin Hu, Haitao Sun, Hongcheng Ni,* Xue-Bin Wang,* Jian Wu, Zhenrong Sun,* and Yan Yang*

Cite This: *J. Phys. Chem. Lett.* 2025, 16, 13271−13276

Read Online

ACCESS | Metrics & More | Article Recommendations | Supporting Information

ABSTRACT: We present direct experimental evidence of ultrafast coupling between ejected electrons and dynamically forming dipole moments in TeO, captured during the photodetachment of TeO^-. By combining high-resolution cryogenic photoelectron spectroscopy with velocity-map imaging, we assess previously inaccessible excited states and resolve rich photoelectron angular distributions (PADs) that encode electron−dipole interactions. Systematic comparison of PADs from femtosecond and picosecond lasers reveals striking deviations from free-electron behavior, representing direct evidence of a transient dipole moment evolving on femtosecond time scales. Quantitative analysis pinpoints the dipole buildup time to be within ∼60 fs, providing real-time access to the birth of a molecular dipole field. This work establishes a general approach to probing electron-dipole interactions in their formation stages, offering fundamental insights into the ultrafast interplay between departing electrons and transient polar systems—a process that lies at the core of atomic, molecular, and ultrafast physics.

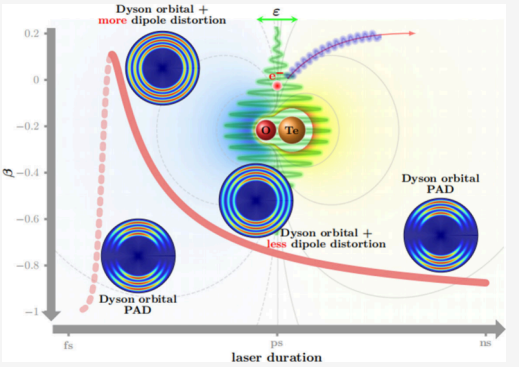

The interaction between electrons and polar molecules underlies fundamental processes from electron scattering to chemical reactivity,[1−3] yet its dynamic aspect, particularly how a transient dipole field emerges and influences departing electrons, remain elusive. While electron-dipole coupling are central to chemical physics, its weak nature renders it difficult to isolate in conventional photoionization, where stronger Coulomb interactions dominate.[4] Photodetachment of molecular anions provides a unique solution: the ejected electron interacts solely with the developing dipole moment of the neutral molecule, free from overwhelming Coulomb effects. Crucially, this anisotropic electron-dipole coupling alters the angular momentum of the departing electron, imprinting its signature on the photoelectron angular distribution (PAD).[5−7] Although static dipole effects have been studied via total cross sections, dipole-bound states, and Feshbach resonances,[8−14] the real-time formation of dipole fields and quantitatively linking PAD modifications to ultrafast electron-dipole interactions remain uncharted territory.

In this work, we leverage the pronounced dipole moment of the neutral counterpart of TeO^- (3.675 D)[15] to directly probe the ultrafast interplay between departing electrons and evolving dipole fields. Using high-resolution cryogenic photoelectron spectroscopy combined with velocity-map imaging (VMI), and by systematically varying laser pulse durations from nanoseconds to femtoseconds, our measurements reveal that electron−dipole coupling builds up within 60 fs. *Ab initio* Dyson orbital[16,17] analyses and time-dependent Schrödinger equation (TDSE) simulations further confirm that this ultrafast interaction takes place on the femtosecond time scale, within which the transient dipole field markedly reshapes the outgoing electron trajectories. Our results establish a direct experimental route to clocking and quantifying the femtosecond-scale buildup of molecular dipoles, providing unprecedented access to the formative stages of fundamental electron-field interactions.

Photodetachment experiments were carried out using the homemade cryogenic anion cluster photoelectron spectroscopy (CRACPES) (Figure S1).[18,19] TeO^- anions were generated by collision-induced dissociation of electrosprayed $HTeO_4^-$ and cooled to 13 K in a 12-pole radio frequency cryogenic ion trap (Figure S2). The resulting cold anions were mass-selected and photodetached using tunable laser pulses with durations ranging from nanoseconds to femtoseconds. Photoelectron images were recorded using a VMI system optimized for cryogenic operation, enabling simultaneous access to photoelectron spectra and angular distributions over a broad energy range.

Figure 1(a) displays the cryogenic photoelectron spectrum of TeO^- recorded at 193 nm (6 ns), revealing three distinct features corresponding to the ground triplet state $X^3\Sigma^{-20}$ and two previously unobserved singlet states $a^1\Delta$ and $b^1\Sigma^+$ of neutral TeO with electron binding energies (eBEs) of 1.76,

Received: September 30, 2025
Revised: December 3, 2025
Accepted: December 8, 2025

https://doi.org/10.1021/acs.jpclett.5c03052
J. Phys. Chem. Lett. 2025, 16, 13271−13276

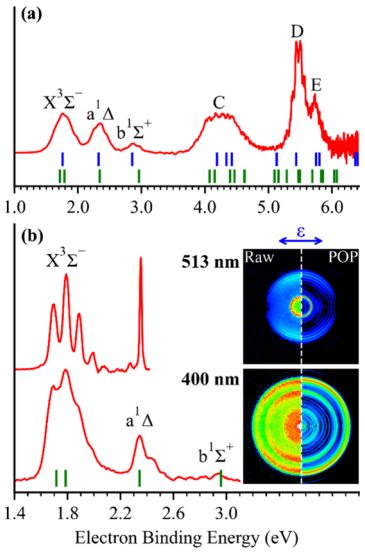

Figure 1. (a) Cryogenic photoelectron spectrum of TeO^- anion at 13 K using a 193 nm laser (6.424 eV, 6 ns). Vertical sticks represent calculated excitation energies of neutral TeO states: spin-excluded (blue) and spin−orbit-coupled (green). (b) VMI spectra of TeO^- anion at 513 nm (2.417 eV, 3.58 ps) and 400 nm (3.100 eV, 60 fs). Left panels of the images show raw images; right panels display results reconstructed from polar onion peeling (POP) algorithm. The blue double arrow indicates laser polarization.

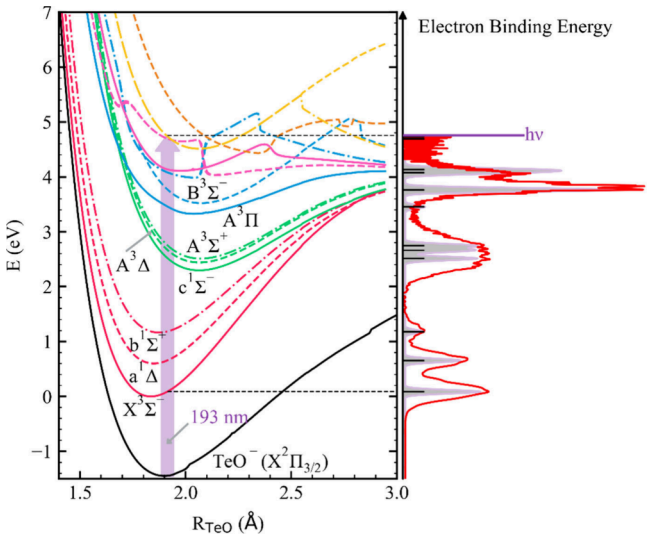

Figure 2. Potential energy curves for the ground state of TeO^- and the low-lying electronic states of neutral TeO, calculated at the NEVPT2[28,29]/aug-cc-pVTZ(-PP) level of theory. Vertical excitation energies (black sticks) are projected onto the eBE axis and overlaid on the experimental spectrum (red curve). Simulated spectrum (gray area) is generated by applying a uniform Gaussian broadening of 30 meV (suitable for high-lying bands, but considerably small for low eBE electrons) to account for the experimental resolution.

2.35, and 2.88 eV, respectively. These measured eBEs match well with high-level theoretical predictions,[15,21] validating the electronic structure assignments. The photoelectron spectrum reveals additional features at higher-energy regions, including a broader band centered at 4.27 eV (labeled as C) and two sharper peaks at 5.50 eV (D) and 5.73 eV (E). Calculated excitation energies [vertical blue sticks in Figure 1(a)] suggest that band C comprises multiple overlapping neutral states, whereas D and E correspond to more complex electronic configurations.

Geometry optimization at the B3LYP-D3(BJ)[22−24]/aug-cc-pVTZ(-PP)[25−27] level yields bond lengths of 1.914 Å for TeO^- ($X^2\Pi_{3/2}$) and 1.837 Å for TeO ($X^3\Sigma^-$) (Figure S3), consistent with prior measurements.[15,20,21] Theoretical adiabatic and vertical detachment energy (ADE and VDE) agree well with the experimental values within 0.07 eV (Table S1). Molecular orbital analyses (Figure S4) and Dyson orbital visualizations (Figure S5) indicate that the X, a, and b states of TeO arise from electron detachment from α- highest occupied molecular orbital (HOMO), β-HOMO, and α-HOMO−1 orbitals of the anion, respectively. These orbitals exhibit pronounced Te-(5s5p)−O(2s2p) hybridization with π^* symmetry (Figure S6), consistent with the observed PAD features discussed below. To unambiguously assign all spectral features, we computed potential energy curves (PECs) for the ground and excited states of TeO and TeO^- (Figure 2). The vertical detachment process at 193 nm, represented by the upward arrow from the minimum of the TeO^- ground state, intersects several TeO PECs, yielding transition energies that align with experimental bands upon Gaussian convolution (fwhm = 30 meV). This treatment provides definitive assignments for nearly all spectral features, facilitating the investigation of subsequent electron dynamics.

To account for relativistic and spin−orbit coupling (SOC) effects critical for heavy elements, we performed spin−orbit-resolved calculations for excited-state energies of TeO. These calculations reveal that the $X^3\Sigma^-$ state splits into two low-lying components of X_10^+ and $X_21^\pm$ separated by 584 cm^{-1}, shown as the first two green sticks in Figure 1(a). While these fine-structure features remain spectrally unresolved at 193 nm due to limited analyzer resolution, their distinct signatures are clearly captured using photoelectron imaging at 513 nm (2.417 eV, 3.58 ps) and 400 nm (3.100 eV, 60 fs) [Figure 1(b)]. The 13 K cooling effectively suppresses hot-band populations in TeO^-, resulting in precise resolution for identifying vibrational structures. The electron affinity (EA, equivalent to the ADE of the anion, defined by the 0−0 vibrational transition), SOC splitting, and vibrational frequency of TeO, are measured directly from the 513 nm spectrum or with multi-Gaussian fitting for 400 nm (Table 1). To assign vibrational progression, we performed Franck−Condon Factor (FCF) simulations for the TeO^- ($X^2\Pi_{3/2}$) → TeO ($X^3\Sigma^-$, $a^1\Delta$) transitions. As shown in Figure 3, the highest computed FCF stick for the $X_21^\pm$ series (blue) is aligned to the strongest peak in the vibrational progression (1.790 eV) due to the double degeneracy of the $X_21^\pm$ state, while the FCFs for the X_10^+ state (green sticks) is assigned by matching to the first vibrational peak (1.696 eV) accordingly. The a2 state (black sticks) exhibits a similar progression, dominated by a strong 0−0 transition. The composite result shows excellent agreement with the experimental VMI spectrum, validating our assignments across both picosecond and femtosecond excitation regimes.

Table 1 compares the key spectroscopic constants of TeO extracted in this work with those from prior studies. The measured EA and vibrational frequency are in good agreement with earlier spectroscopic results.[15,20,21,30−34] The measured SOC splitting is consistent with reported values,[31,33,34] though our calculations underestimate this splitting by ∼176 cm^{-1}. Importantly, the SOC splitting and vibrational frequency are of comparable magnitude (∼770 cm^{-1}), resulting in substantial overlap between the (ν+1) level of X_10^+ and (ν) level of $X_21^\pm$

https://doi.org/10.1021/acs.jpclett.5c03052
J. Phys. Chem. Lett. 2025, 16, 13271−13276

Table 1. EA, SOC Splitting, and Vibrational Frequency of TeO ($X^3\Sigma^-$) from This Work, Compared with Prior Studies

	Vibrational Freq (cm^{-1})						
	Expt.		Calc.		SOC (cm^{-1})		
EA (eV) $X_1 0^+$	$X_1 0^+$	$X_2 1^\pm$	$X_1 0^+$	$X_2 1^\pm$	Expt.	Calc.	
1.696 ± 0.014	772 ± 50		811[a]		760 ± 50	584[b]	VMI@513 nm
1.696 ± 0.030	793 ± 50				780 ± 60		VMI@400 nm
1.697[c]	~790[c]		802[i]	801[i]	750[c]	923[i]	
	797.69,[d] 797.70[d]		811[j]	809[j]	781.75[e]	793[j]	
	798.030,[e] 797.821[e]				789[g]		
	797.11,[f] 797.821[f]				679[h]		

[a]Calculated at the B3LYP-D3(BJ)/aug-cc-pVTZ(-PP) level. [b]Calculated at the NEVPT2/aug-cc-pVTZ-DK level. [c]Reference 20. [d]Reference 30. [e]Reference 31. [f]Reference 32. [g]Reference 33. [h]Reference 34. [i]Reference 21. [j]Reference 15.

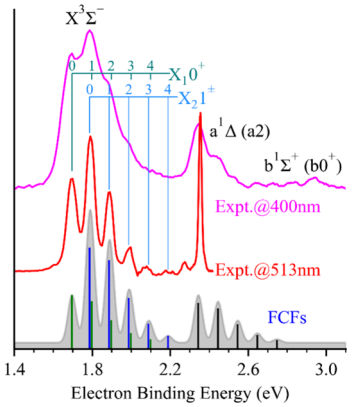

Figure 3. VMI spectra and calculated FCF sticks spectra ($X_1 0^+$ green, $X_2 1^\pm$ blue, a2 black). The simulated spectrum on the bottom (gray filled curve) was obtained by summing the three sets of stick spectra, convolved with a 50 meV Gaussian width broadening to match the experimental resolution.

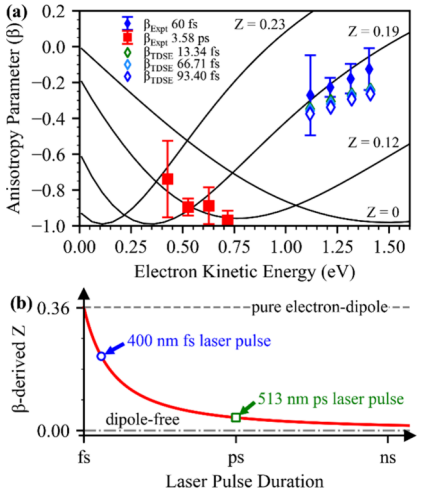

Figure 4. (a) The β values of the PADs obtained from the 400 nm fs pulse and 513 nm ps pulse experiments as a function of eKE. The multicenter treatment β curves were computed using the EOM-IP-CCSD Dyson orbitals (Figure S6) of the $X^3\Sigma^-$ state, with Z charges labeled. TDSE (◊) calculated β values under femtosecond for the respective eKE electrons are also shown. More detailed analyses of β value vs eKE and its dependencies on Z charges including $a^1\Delta$state are provided in Figure S8. (b) Schematic illustration of the pulse duration dependent evolution of the β-derived Z value.

within the experimental energy resolution (~113 cm^{-1}). Despite this overlap, these levels were successfully differentiated through the detailed FCF analyses.

The PAD was quantified through Abel-inverted spectrum using the standard expression for one-photon detachment:[35,36]

$$I(\theta) \propto 1 + \beta P_2(\cos\theta)$$

where β is the anisotropy parameter (ranging from −1 to 2), P_2 is the second-order Legendre polynomial, and θ is the polar angle denoting photoelectron emission direction with respect to the quantization axis of laser polarization direction. Through this analysis, we determined vibrationally resolved β parameters for different electronic states (Table S2).

Initial theoretical predictions using plane-wave expansion based on Dyson orbitals failed to reproduce the experimental anisotropy parameter β, highlighting the inadequacy of dipole-free treatments (shown in Figure S7). Following prior studies on SO^- and CN^- conducted by Hart et al. and Ru et al.,[5,6] we incorporated electron-dipole interactions via a multicenter Coulomb wave expansion,[37] assigning effective point charges ± Z to the Te (+Z) and O (-Z) atomic sites of neutral TeO, generating an effective dipole moment while maintaining overall charge neutrality. The resulting β parameters, shown in Figure 4(a) (gray curves), exhibit pronounced sensitivity to the effective charge parameter Z.

Crucially, we observe that fitted Z values depend on both the final electronic state and the laser pulse duration. For femtosecond pulses (400 nm), optimal Z values are significantly larger (0.19 for $X^3\Sigma^-$, 0.23 for $a^1\Delta$) than those derived from picosecond pulses (513 nm: Z = 0.12 and 0, respectively). The observed variation in effective charge cannot be explained by intensity effects, as the ponderomotive energy remains negligible under our experimental conditions (see calculations in section 2.3 of the Supporting Information). Furthermore, the influence of electron kinetic energy (eKE) can be excluded as a primary contributing factor. Both the $X^3\Sigma^-$ state at 513 nm and the $a^1\Delta$state at 400 nm exhibit comparable eKEs and nearly identical Dyson orbitals (Figures S5 and S8). Despite these similarities, the experimentally determined β parameters differ substantially, with β(fs) approximately −0.35 and β(ps) approximately −0.93.

Rather, these differences directly reflect the femtosecond-scale emergence of the dipole field and its subsequent temporal averaging over the measurement window, as shown in Figure 4(b). The systematic discrepancy of Z values from the pure electron-dipole case provides compelling evidence for the dynamic nature of the dipole formation process, where the measured Z values capture the transient dipole field during its formative stage rather than the fully developed static dipole moment. Specifically, all experimentally derived Z values are

https://doi.org/10.1021/acs.jpclett.5c03052
J. Phys. Chem. Lett. 2025, 16, 13271−13276

significantly smaller than those predicted by either static dipole moments (∼0.36) or CM5 population analysis (0.361)[38] (Tables S3 and S4). These predicted values represent the theoretical upper bound of the electron-dipole interaction influence on the PAD, as illustrated by the dashed curve (pure electron-dipole) in Figure 4(b). Furthermore, the presence of the laser field causes the PAD to progressively converge toward the dipole-free scenario [dot-line in Figure 4(b)] as the pulse duration increases. Notably, the fitted Z values obtained with 400 nm femtosecond pulses fall between the two limiting cases, indicating that the electron−dipole interaction is attenuated on the ∼ 60 fs time scale of the laser pulse. This result shows that, under our experimental conditions, dipole formation must occur within the 60 fs duration of the laser pulse; otherwise, the full electron−dipole interaction (Z = 0.36) would have been observed.

To directly capture the femtosecond-scale temporal evolution of electron-dipole interaction during photodetachment, we performed full numerical TDSE simulations of photoelectron wave packet dynamics in the presence of an emergent dipole field.[39] The system was initialized at the equilibrium nuclear geometry of TeO^-, with Dyson-like initial wave function constructed via imaginary-time propagation.[40] For the picosecond regime, we employed the lowest-order perturbation theory (LOPT) that neglects nuclear motion. For the femtosecond regime, the initial wave function was evolved within the full time-dependent Hamiltonian including the laser field using the split-operator Fourier method, and the final PAD was extracted from the photoelectron momentum distribution after the conclusion of the laser field (see Supporting Information for details). In both femtosecond and picosecond cases, identical Dyson orbitals served as the initial electronic wave function, and the PADs were computed by averaging over all molecular orientations (0° to 180° in 5° increments).

As illustrated in Figure 4(a), the TDSE simulations reveal a striking temporal evolution in the photoelectron anisotropy β (hollow diamonds). The calculated β values show excellent agreement with experimental results while exhibiting a clear monotonic decrease with increasing pulse duration. This trend directly reflects the ultrafast onset and evolution of electron−dipole interactions during photodetachment. Remarkably, our analysis demonstrates that the electron-dipole interaction becomes effective within tens of femtoseconds following electron detachment, corroborating the 60 fs time scale that determined jointly by the laser pulse duration and the above multicenter treatment analyses. This highlights both the prompt polarization response of the neutral TeO fragment and the ultrafast establishment of its internal dipole field. These findings underscore the temporal sensitivity of PADs to evolving molecular fields.

The comparison to the effective charge (Z) extracted from the multicenter Coulomb model further corroborates this picture. Under femtosecond pulses, larger Z values are required to reproduce both experimental and TDSE-calculated β values (hollow diamonds), indicating stronger anisotropic interactions than from a well-established static dipole field. In contrast, under picosecond excitation, the effective charge Z is significantly smaller and approaches zero, and all the LOPT calculated β values (Figure S9) converge to those predicted by the dipole-free model. This systematic variation demonstrates that the field's anisotropic effect is progressively averaged out over 'longer' interaction time window, thus suppressing its influence on the PAD. Notably, the residual dipole effect with Z = 0.12 observed even under picosecond laser pulse indicates that complete elimination of the dipole effect is unattainable, highlighting the persistent influence of dipole interactions. Overall, the laser pulse manifests as a tunable temporal filter for dipole interactions in the PAD, enabling systematic separation of dynamic electron-dipole interactions through controlled variation of the experimental time scale of the pulse duration.

These findings reflect a fundamental interplay between the real-time formation of a molecular dipole field and the temporal structure of the probe itself. The Dyson orbital and eKE determine the intrinsic PAD of the photodetached electrons. Once the electron is detached, the rapidly forming dipole moment of the neutral molecule directly modifies this distribution, rendering the PAD more isotropic. Our experiments and theoretical calculations demonstrate that the laser field can partially counteract this effect: the PAD observed with femtosecond excitation [fitted $\beta(Z = 0.19)$] is closer to the dipole-induced limit [$\beta(Z = 0.36)$], whereas that with picosecond excitation [fitted $\beta(Z = 0.12)$] approaches the intrinsic PAD [$\beta(Z = 0)$]. In physical terms, each photodetachment event is ultrafast, and the emitted electron samples the instantaneous dipole of the neutral. In long pulses, electrons are produced across a broad range of emission times; although each electron experiences a similar dipole magnitude, the dipole-induced phases are not phase-locked. The resulting incoherent average over emission times cancels the dipole-dependent interaction, inducing the nearly field-free angular distribution. Therefore, the laser pulse, beyond triggering the detachment, also acts as a temporal gate that determines how much of the dipole-induced modification can be encoded and "seen" by the observer. In this sense, the PAD becomes not only a probe of internal dynamics, but also a recorder of when and how these dynamics couple to the outgoing electrons. This dual sensitivity establishes photodetachment PADs as a unique probe for time-resolving weak interactions in the presence of dominant Coulomb effects.

In summary, we report a time-resolved picture of electron−dipole interactions in photodetaching a polar molecular anion of TeO^- beyond revealing new excited states of TeO. Through systematic comparison of PADs under femtosecond and picosecond laser excitation, we experimentally resolve a 60 fs buildup time of the dipole moment of TeO and its influence on electron emission patterns. The quantitative agreement among multicenter modeling, TDSE simulations, and experimental anisotropic β parameters establish a complete picture of how transient dipole fields imprint their signature on photoelectron wave packets, marking the first direct measurement of the spatiotemporal structure of dipolar molecular fields acting on free electrons. Importantly, this study uncovers how subtle electron−dipole coupling can be masked or revealed depending on specific measurement settings, offering insight into the interplay between intrinsic dynamics and experimental observables. This work therefore lay out a framework for probing weak field-mediated processes with femtosecond resolution and highlights PAD as a sensitive spectroscopic tool to interrogate fundamental electron−field interactions beyond Coulombic regimes.

https://doi.org/10.1021/acs.jpclett.5c03052
J. Phys. Chem. Lett. 2025, 16, 13271−13276

■ ASSOCIATED CONTENT

Supporting Information

The Supporting Information is available free of charge at https://pubs.acs.org/doi/10.1021/acs.jpclett.5c03052.

Experimental and theoretical methods, additional results, schematic diagram of experimental system, mass spectrum spectrum, optimized structures, molecular orbitals, Dyson orbital, schematic diagram of electronic configuration, photoelectron anisotropy parameter with expansion the plane-wave treatment, photoelectron anisotropy parameter with expansion the multicenter treatment, photoelectron anisotropy parameter with LOPT method, experimental and calculated VDEs and ADE, experimental anisotropy parameter, population analysis of atomic charges, and dipole moment of TeO (PDF)

■ AUTHOR INFORMATION

Corresponding Authors

Hongcheng Ni − *State Key Laboratory of Precision Spectroscopy, School of Physics and Electronic Science, East China Normal University, Shanghai 200241, China; Collaborative Innovation Center of Extreme Optics, Shanxi University, Taiyuan, Shanxi 030006, China;* orcid.org/0000-0003-4924-0921; Email: hcni@lps.ecnu.edu.cn

Xue-Bin Wang − *Physical Sciences Division, Pacific Northwest National Laboratory, Richland, Washington 99352, United States;* orcid.org/0000-0001-8326-1780; Email: xuebin.wang@pnnl.gov

Zhenrong Sun − *State Key Laboratory of Precision Spectroscopy, School of Physics and Electronic Science, East China Normal University, Shanghai 200241, China; Collaborative Innovation Center of Extreme Optics, Shanxi University, Taiyuan, Shanxi 030006, China*; Email: zrsun@phy.ecnu.edu.cn

Yan Yang − *State Key Laboratory of Precision Spectroscopy, School of Physics and Electronic Science, East China Normal University, Shanghai 200241, China;* orcid.org/0000-0003-3769-693X; Email: yyang@lps.ecnu.edu.cn

Authors

Fan Yang − *State Key Laboratory of Precision Spectroscopy, School of Physics and Electronic Science, East China Normal University, Shanghai 200241, China*

Haomai Hou − *State Key Laboratory of Precision Spectroscopy, School of Physics and Electronic Science, East China Normal University, Shanghai 200241, China*

Jian Zhang − *College of Chemistry and Chemical Engineering, Donghua University, Shanghai 201620, China*

Xueying Li − *State Key Laboratory of Precision Spectroscopy, School of Physics and Electronic Science, East China Normal University, Shanghai 200241, China*

Peng Tang − *State Key Laboratory of Precision Spectroscopy, School of Physics and Electronic Science, East China Normal University, Shanghai 200241, China*

Ye Mei − *State Key Laboratory of Precision Spectroscopy, School of Physics and Electronic Science, East China Normal University, Shanghai 200241, China;* orcid.org/0000-0002-3953-8508

Junyang Ma − *State Key Laboratory of Precision Spectroscopy, School of Physics and Electronic Science, East China Normal University, Shanghai 200241, China;* orcid.org/0009-0005-1778-2576

Zhubin Hu − *State Key Laboratory of Precision Spectroscopy, School of Physics and Electronic Science, East China Normal University, Shanghai 200241, China*

Haitao Sun − *State Key Laboratory of Precision Spectroscopy, School of Physics and Electronic Science, East China Normal University, Shanghai 200241, China;* orcid.org/0000-0003-1471-8876

Jian Wu − *State Key Laboratory of Precision Spectroscopy, School of Physics and Electronic Science, East China Normal University, Shanghai 200241, China; Collaborative Innovation Center of Extreme Optics, Shanxi University, Taiyuan, Shanxi 030006, China;* orcid.org/0000-0002-1318-2291

Complete contact information is available at: https://pubs.acs.org/10.1021/acs.jpclett.5c03052

Author Contributions

The manuscript was written through contributions of all authors. All authors have given approval to the final version of the manuscript.

Notes

The authors declare no competing financial interest.

■ ACKNOWLEDGMENTS

The work was partly supported by the National Natural Science Foundation of China (Grants No. 12034008, No. 12250003, No. 92461301, and No. 12474341). X.-B.W. was supported by U.S. Department of Energy (DOE), Office of Science, Office of Basic Energy Sciences, Division of Chemical Sciences, Geosciences, and Biosciences, Condensed Phase and Interfacial Molecular Science program, FWP 16248.

■ ABBREVIATIONS

PAD	photoelectron angular distribution
VMI	velocity-map imaging
TDSE	time-dependent Schrödinger equation
POP	polar onion peeling
CRACPES	cryogenic anion cluster photoelectron spectroscopy
eBE	electron binding energies
PEC	potential energy curve
SOC	spin−orbit coupling
EA	electron affinity
FCF	Franck−Condon factor
LOPT	lowest-order perturbation theory
eKE	electron kinetic energy
HOMO	highest occupied molecular orbital
ADE	adiabatic detachment energy
VDE	vertical detachment energy.

■ REFERENCES

(1) Rybicka-Jasińska, K.; Vullev, V. I. Molecular electrets − Why do dipoles matter for charge transfer and excited-state dynamics? *J. Photochem. Photobiol., A* **2020**, *401*, 112779.

(2) Hotop, H.; Rul, M.-W.; Fabrikant, I. I. Resonance and Threshold Phenomena in Low-Energy Electron Collisions with Molecules and Clusters. *Phys. Scr.* **2004**, *110*, 22.

(3) Fabrikant, I. I. Long-range effects in electron scattering by polar molecules. *Journal of Physics B: Atomic, Molecular and Optical Physics* **2016**, *49* (22), 222005.

(4) Griffiths, D. J. *Introduction to Electrodynamics*; Cambridge University Press: 2017.
(5) Hart, C. A.; Lyle, J.; Spellberg, J.; Krylov, A. I.; Mabbs, R. Role of the Electron-Dipole Interaction in Photodetachment Angular Distributions. *J. Phys. Chem. Lett.* **2021**, *12* (41), 10086−10092.
(6) Ru, B.; Hart, C. A.; Mabbs, R.; Gozem, S.; Krylov, A. I.; Sanov, A. Dipole effects in the photoelectron angular distributions of the sulfur monoxide anion. *Phys. Chem. Chem. Phys.* **2022**, *24*, 23367−23381.
(7) Dowek, D.; Decleva, P. Trends in angle-resolved molecular photoelectron spectroscopy. *Phys. Chem. Chem. Phys.* **2022**, *24* (40), 24614−24654.
(8) Simpson, M.; Nötzold, M.; Michaelsen, T.; Wild, R.; Gianturco, F. A.; Wester, R. Influence of a Supercritical Electric Dipole Moment on the Photodetachment of C_3N^-. *Phys. Rev. Lett.* **2021**, *127* (4), 043001.
(9) Hlousek, B. A.; Martin, M. F.; Khakoo, M. A.; Zawadzki, M.; Moreira, G. M.; Maioli, L. S.; Bettega, M. H. F.; Machado, L. E.; da Mata, V. A. S.; da Silva, A. J.; et al. Elastic scattering of electrons from chloroform. *Phys. Rev. A* **2019**, *100* (5), 052709.
(10) Gallup, G. A.; Fabrikant, I. I. Vibrational Feshbach resonances in dissociative electron attachment to uracil. *Phys. Rev. A* **2011**, *83* (1), 012706.
(11) Zhang, Y.-R.; Yuan, D.-F.; Wang, L.-S. Probing Dipole-Bound States Using Photodetachment Spectroscopy and Resonant Photoelectron Imaging of Cryogenically Cooled Anions. *J. Phys. Chem. Lett.* **2023**, *14* (33), 7368−7381.
(12) Kunin, A.; Neumark, D. M. Time-resolved radiation chemistry: femtosecond photoelectron spectroscopy of electron attachment and photodissociation dynamics in iodide−nucleobase clusters. *Phys. Chem. Chem. Phys.* **2019**, *21* (14), 7239−7255.
(13) Verlet, J. R. R.; Anstöter, C. S.; Bull, J. N.; Rogers, J. P. Role of Nonvalence States in the Ultrafast Dynamics of Isolated Anions. *J. Phys. Chem. A* **2020**, *124* (18), 3507−3519.
(14) Kang, D. H.; Kim, J.; Eun, H. J.; Kim, S. K. State-Specific Chemical Dynamics of the Nonvalence Bound State of the Molecular Anions. *Acc. Chem. Res.* **2022**, *55* (20), 3032−3042.
(15) Chattopadhyaya, S.; Nath, A.; Das, K. K. Effects of spin−orbit coupling on the electronic states and spectroscopic properties of tellurium monoxide molecule - A theoretical study. *Computational and Theoretical Chemistry* **2016**, *1084*, 75−87.
(16) Melania Oana, C.; Krylov, A. I. Dyson orbitals for ionization from the ground and electronically excited states within equation-of-motion coupled-cluster formalism: Theory, implementation, and examples. *J. Chem. Phys.* **2007**, *127* (23), 234106.
(17) Oana, C. M.; Krylov, A. I. Cross sections and photoelectron angular distributions in photodetachment from negative ions using equation-of-motion coupled-cluster Dyson orbitals. *J. Chem. Phys.* **2009**, *131* (12), 124114.
(18) Tang, P.; Zhang, J.; Li, X.; Yang, F.; Zhao, Q.; Ma, J.; Hu, Z.; Sun, H.; Wang, X.-B.; Sun, Z.; et al. Cryogenic Photoelectron Spectroscopic and Theoretical Study of the Electronic and Geometric Structures of Undercoordinated Osmium Chloride Anions $OsCl_n^-$ (n = 3−5). *J. Phys. Chem. A* **2024**, *128* (28), 5500−5507.
(19) Zhao, Q.; Zhang, J.; Li, X.; Tang, P.; Yang, F.; Ma, J.; Hu, Z.; Sun, H.; Wang, X.-B.; Sun, Z.; et al. Exploring direct photodetachment and photodissociation−photodetachment dynamics of platinum iodide anions (PtI_n^-, n = 2−5) using cryogenic photoelectron spectroscopy. *J. Chem. Phys.* **2024**, *161* (21), 214305.
(20) Freidhoff, C. B.; Coe, J. V.; Snodgrass, J. T.; McHugh, K. M.; Bowen, K. H. Negative ion photoelectron spectroscopy of TeO^-. *Chem. Phys. Lett.* **1986**, *124* (3), 268−273.
(21) Rai-Constapel, V.; Liebermann, H.-P.; Buenker, R. J.; Rai, S. N. Ab Initio MRD-CI Study of the Spectrum of the TeO Molecule Employing Relativistic Effective Core Potentials. *J. Phys. Chem. A* **2006**, *110* (2), 404−411.
(22) Stephens, P. J.; Devlin, F. J.; Chabalowski, C. F.; Frisch, M. J. Ab Initio Calculation of Vibrational Absorption and Circular Dichroism Spectra Using Density Functional Force Fields. *J. Chem. Phys.* **1994**, *98* (45), 11623−11627.
(23) Grimme, S.; Antony, J.; Ehrlich, S.; Krieg, H. A consistent and accurate ab initio parametrization of density functional dispersion correction (DFT-D) for the 94 elements H-Pu. *J. Chem. Phys.* **2010**, *132* (15), 154104.
(24) Grimme, S.; Ehrlich, S.; Goerigk, L. Effect of the damping function in dispersion corrected density functional theory. *J. Comput. Chem.* **2011**, *32* (7), 1456−1465.
(25) Dunning, T. H. Gaussian basis sets for use in correlated molecular calculations. I. The atoms boron through neon and hydrogen. *J. Chem. Phys.* **1989**, *90*, 1007−1023.
(26) Kendall, R. A.; Dunning, T. H.; Harrison, R. J. Electron affinities of the first-row atoms revisited. Systematic basis sets and wave functions. *J. Chem. Phys.* **1992**, *96*, 6796−6806.
(27) Peterson, K. A.; Figgen, D.; Goll, E.; Stoll, H.; Dolg, M. Systematically convergent basis sets with relativistic pseudopotentials. II. Small-core pseudopotentials and correlation consistent basis sets for the post-d group 16−18 elements. *J. Chem. Phys.* **2003**, *119* (21), 11113−11123.
(28) Angeli, C.; Cimiraglia, R.; Evangelisti, S.; Leininger, T.; Malrieu, J. P. Introduction of n-electron valence states for multireference perturbation theory. *J. Chem. Phys.* **2001**, *114* (23), 10252−10264.
(29) Angeli, C.; Cimiraglia, R.; Malrieu, J.-P. n-electron valence state perturbation theory: A spinless formulation and an efficient implementation of the strongly contracted and of the partially contracted variants. *J. Chem. Phys.* **2002**, *117* (20), 9138−9153.
(30) Chandler, G. G.; Hurst, H. J.; Barrow, R. F. Rotational analysis of the A − X system of tellurium monoxide. *Proceedings of the Physical Society* **1965**, *86* (1), 105−248.
(31) Setzer, K. D.; Fink, E. H. The $b^1\Sigma^+(b0^+) \rightarrow X^3\Sigma^-(X_10^+, X_21)$ and $a^1\Delta(a2) \rightarrow X^3\Sigma^-(X_21)$ transitions of TeO. *J. Mol. Spectrosc.* **2014**, *295*, 21−25.
(32) Huber, K. P.; Herzberg, G. *Molecular spectra and molecular structure: IV. Constants of diatomic molecules*; Springer Science & Business Media: 1979.
(33) Winter, R.; Barnes, I.; Fink, E. H.; Wildt, J.; Zabel, F. $b^1\Sigma^+$ and $a^1\Delta$ emissions from group VI-VI diatomic molecules: $b0^+ \rightarrow X_10^+$, X_21 emissions of TeO and TeS. *J. Mol. Struct.* **1982**, *80*, 75−82.
(34) Barrow, R. F.; Hutchings, M. R. The Ω=1,0^+ separation in the $^3\Sigma^-$ ground state of gaseous TeO. *Journal of Physics B: Atomic and Molecular Physics* **1972**, *5* (6), L132.
(35) Reid, K. L. Photoelectron Angular Distributions. *Annu. Rev. Phys. Chem.* **2003**, *54*, 397−424.
(36) Cooper, J.; Zare, R. N. Angular Distribution of Photoelectrons. *J. Chem. Phys.* **1968**, *48* (2), 942−943.
(37) Gozem, S.; Seidel, R.; Hergenhahn, U.; Lugovoy, E.; Abel, B.; Winter, B.; Krylov, A. I.; Bradforth, S. E. Probing the Electronic Structure of Bulk Water at the Molecular Length Scale with Angle-Resolved Photoelectron Spectroscopy. *J. Phys. Chem. Lett.* **2020**, *11* (13), 5162−5170.
(38) Marenich, A. V.; Jerome, S. V.; Cramer, C. J.; Truhlar, D. G. Charge Model 5: An Extension of Hirshfeld Population Analysis for the Accurate Description of Molecular Interactions in Gaseous and Condensed Phases. *J. Chem. Theory Comput.* **2012**, *8* (2), 527−541.
(39) Wolkow, D. M. Über eine Klasse von Lösungen der Diracschen Gleichung. *Zeitschrift für Physik* **1935**, *94* (3−4), 250−260.
(40) Lehtovaara, L.; Toivanen, J.; Eloranta, J. Solution of time-independent Schrödinger equation by the imaginary time propagation method. *J. Comput. Phys.* **2007**, *221* (1), 148−157.

https://doi.org/10.1021/acs.jpclett.5c03052
J. Phys. Chem. Lett. 2025, 16, 13271−13276